

Reply to the comments of Reviewer No. 1

Levin Klein on behalf of the authors
IAG, University of Stuttgart

August 29, 2018

The authors would like to thank the reviewer for his/her efforts and constructive comments again. They are very much appreciated and incorporated into the revised manuscript.

In this document the comments given by the 1st reviewer are addressed consecutively. The following formatting is chosen:

- The reviewer comments are marked in blue and italic.
- The reply by the authors is in black color.
- A marked-up manuscript is added. Changed sections with regard to the comments by reviewer 1 are marked in yellow.

Minor comments "Mi"

1. *"2.3.2 - Mesh deformation -> The authors stated that surfaces in the CFD domain are deformed following the marker displacements. In the referee's opinion, the internal CFD domain must be deformed to follow the moving surfaces: how does the deformation library handle with this aspect? Could the author add a sentence that explains how the deformation is distributed within the CFD domain?"*

The volume meshes (internal CFD domains) are deformed based on the surface mesh deformation using radial basis function. This has already been stated at the end of the section.

2. *"2.3.3 - Load integration -> In the paragraph the authors wrote: "For the coupling to SIMPACK, the CFD surface is divided into segments based on the deformed marker positions. Loads are integrated for these segments and assigned to the respective markers." Could the authors explain more in detail how a CFD segment area is assigned to a single marker. Do the authors use a sort of reduction technique?"*

While detailed distribution of loads in form of surface pressure and friction is available in the CFD simulation, forces can only be applied at discrete positions/points in the structural model. This is explained in section 2.3.1. As written in section 2.3.3 the CFD surface is divided into segments based on the the deformed positions of these markers. Pressure and frictions are integrated over the segments and the resulting loads are assigned to the respective markers. The authors revised the section mentioned by the reviewer to make this clearer, see **R1:Mi2** (page 5, line 148)

3. *"2.3.4 - Communication interface -> The authors employed a typical coupling scheme between Simpack and FLOWer code, yet the two solvers run on different operating systems and the data communication must be handle by means of files. According to the referee, this strategy*

may lengthen the computational time due to writing and reading time. Would it be possible to run the two solvers on the same cluster exchanging information, for instance, by using an Infiniband connection? Do the authors have an idea of the time reduction in case the solvers exchange conditions by network instead of using files?"

The reading and writing time is very fast, each communication takes approx 0.1 second which is much less than 1% of the time for one time step (approx. 40 seconds) as the files are really small (approx. 22kB each in case LC2_FSC3). One big advantage of using files is, that no connection between the solvers has to be established, thus *SIMPACK* can just wait for files from *FLOWer* while *FLOWer* is restarted (due to limited job duration on clusters). Furthermore, *SIMPACK* runs only on specific Linux distributions which are not available on most clusters.

4. *"2.5.2 - CFD model -> The authors show a detail of the computational grid (Figure 3), yet it would be nice if they may add a picture of the overall CFD domain. The authors mention that the fine mesh consists of 86 M of cells and a picture showing the entire domain may highlight this huge computational domain."*

The authors understand that a figure of the computational domain would be nice, but actually it makes no sense to create such a figure including the mesh or cuts through the mesh. Compared to the size of the computational domain (≈ 3 kilometre) even the resolution of the background mesh is too fine and would just result in black areas in most parts of the figure. Furthermore, the second reviewer recommended to shorten the paper and to remove less important figures.

5. *"2.6 - Evaluation -> The referee agrees that the temporal resolution is strictly commented to the time step. Could the author add the highest frequency solved in the analyses? The author also said "To achieve the same temporal resolution in the acoustic emission, each time step a CFD surface solution was saved as input for the acoustic simulations" and all these information may require a huge amount of disk storage, how do the authors face this aspect? Finally, at the end of the paragraph the authors state that they apply FFT algorithm to the period solution: how do they check the solution periodicity?"*

The authors added the Nyquist frequency as highest resolved frequency, which is known as half the sampling rate, see **R1:Mi5-a** (page 11, line 284).

The surface files were only temporally on the cluster and deleted after the acoustic simulation was finished. This requires approx. 8.6 Gigabyte per revolution which can easily be handled with the available resources. The authors added "temporally" to the sentence cited by the reviewer, see **R1:Mi5-b** (page 11, line 273)

Most effects on the turbine are periodic to or occur periodically with the rotation frequency or the blade passing frequency (tower passage, gravitational forces, sheared inflow). Thus, a whole-numbered number of turbine revolutions was chosen for the evaluation.

6. *"3 - Results -> The authors clearly discussed the three different studies and all the explanations are described in detail. Focusing on acoustic emissions, the authors concluded that a) the main source of noise turns out to be the blade-tower interaction, b) it is important to consider the elastic deformation which reduce the gap between blade and tower and c) the turbulence inflow only alters the broadband noise level. The authors show the noise results in term of SPL in observer positions, would it be possible to compute a PWL (sound power level) value from the results to have a global quantity describing the acoustic energy and to globally compare the different cases annoyance at a certain distance from the wind turbine?"*

PWL results from integration over a surface surrounding the acoustic source and thus is independent of the distance and yields no information about directivity and tonality. In the eyes of the authors it is not suitable to compare annoyance of the different cases which is often associated with tonal noise.

7. *"In the paper the authors often write "acoustic immission". The referee thinks that is was a typo and the authors would have like to write "acoustic emissions". Please revise it in the paper."*

The authors also discussed this topic. They think, that immission is the right word. Emission describes everything that's emitted from the source (turbine). At a specific observer position only the immission can be measured. The approach in the paper is to compare the immissions at the observer positions and draw a conclusion on how the emission of the turbine change.

Advanced CFD-MBS coupling to assess low-frequency emissions from wind turbines

Levin Klein¹, Jonas Gude¹, Florian Wenz¹, Thorsten Lutz¹, and Ewald Krämer¹

¹Institute of Aerodynamics and Gas Dynamics, University of Stuttgart, Pfaffenwaldring 21, 70569 Stuttgart, Germany

Correspondence: Levin Klein (levin.klein@iag.uni-stuttgart.de)

Abstract. The low-frequency emissions from a generic 5 MW **R2:AC1** wind turbine are investigated numerically. In order to regard airborne noise and structure-borne noise simultaneously a process chain was developed. It considers fluid-structure coupling (FSC) of a computational fluid dynamics (CFD) solver and multibody simulations (MBS) solver as well as a Ffowcs Williams-Hawkings (FW-H) acoustic solver. The approach was applied to a generic 5 MW turbine to get more insight into the sources and mechanisms of low-frequency emissions from wind turbines. For this purpose simulations with increasing complexity in terms of considered components in the CFD model, degrees of freedom in the structural model and inflow in the CFD model were conducted. Consistent with literature, it has been found that aeroacoustic low-frequency emission is dominated by the blade-passing frequency harmonics. ~~The tower base loads, which excite seismic emission, tend to be dominated by structural eigenfrequencies with increasing complexity of the model. The~~ **R2:AC2** In the spectra of the tower base loads, which excite seismic emission, the structural eigenfrequencies become more prominent with increasing complexity of the model. The main source of **R2:AC3** low-frequency aeroacoustic emissions is the blade-tower interaction and the contribution of the tower as an acoustic emitter is stronger than the contribution of the rotor. Aerodynamic tower loads also significantly contribute to the external excitation acting on the structure of the wind turbine.

1 Introduction

Renewable sources of energy and especially wind power have seen a strong expansion in the last years. Even though the construction of large offshore wind farms is currently a strong focus, the potential of onshore wind turbines by opening up new, previously unused areas and repowering of existing sites is still significant. With regard to the acceptance and the fulfillment of stricter legal requirements concerning noise and vibrations, the research on low-frequency emissions from wind turbines gains importance.

1.1 **R2:C1-a** Emissions from wind turbines

As wind turbines are counted among the tallest machines on the planet that work in an uncontrolled outside environment, noise and vibration emissions **R2:AC4** occur in a broad frequency range ~~occur~~. While sources of acoustic wind turbine emission in the audible range are widely researched, **R2:AC5** and understood and different methods are applied to reduce aerodynamic and mechanical noise (Liu, 2017), there is much less known about low-frequency emissions from wind turbines. Many publi-

25 cations about low-frequency emissions of **Authors** from wind turbines concentrate on the impact on seismic measurements.
26 The emitted ground motion signals from wind turbines are measured by local seismic stations built for detection of events
27 with small magnitudes like far away earthquakes or nuclear weapons tests. Zieger and Ritter (2018) observed an increase of
28 amplitudes in a frequency range from 0.5 Hz to 10 Hz dependent of the rotational speed of the turbine and thus wind speed at
29 a distance of 5.5 km away from a wind turbine. This confirms the measurements by Stammler and Ceranna (2016) and Styles
30 et al. (2005) who found that nearby wind turbines reduce the sensitivity of seismic stations as they introduce wind dependence
31 into the measured noise spectra.

32 Acoustic measurements in the low-frequency range 3.3 km from a wind farm show discrete peaks at the blade-passing fre-
33 quency (BPF) and its higher harmonics below 20 Hz (Hansen et al., 2017). This was also observed by Pilger and Ceranna
34 (2017) who evaluated the data obtained by a microbarometer array for infrasound detection located in northern Germany.
35 ~~Zajamšek et al. (2016) investigated the measurability of these acoustic waves in buildings. Zajamšek et al. (2016)~~ **R2:AC6**
36 compared outdoor and indoor measurements close to an Australian wind farm and found the same tonal character in the
37 noise spectra. Hence, the blade-tower interaction is seen to be responsible for aeroacoustic low-frequency noise of wind farms
38 **Authors** wind farms (Van den Berg, 2005).

39 **R2:AC7** The scope of research on low-frequency noise from wind turbines is often its impact on human beings. Knopper
40 et al. (2014) conclude from their literature survey that human health is not likely to be affected by low-frequency noise and
41 infrasound from wind turbines. Turnbull et al. (2012) state that the measured level of infrasound within two Australian wind
42 farms was similar to that measured in urban and coastal areas and near other engineered noise sources.

43

44 1.2 **R2:C1-b** Numerical approaches on low frequency noise

45 For an optimization of the structure and foundations of future wind turbines as well as for the assessment of the impact of low-
46 frequency noise and low-frequency seismic vibrations on the environment, reliable methods for the prediction of emissions
47 are of great importance. Gortsas et al. (2017) performed a numerical study to calculate wave propagation using the Boundary
48 Element Method. They developed a model which considers the mentioned seismic vibrations as well as the low-frequency
49 noise in air and even allows a prediction of the sound pressure level (SPL) inside a generic building. But, as this model is only
50 capable to calculate the propagation, reliable input data representing the airborne and structure-borne emissions from the wind
51 turbine has to be provided. CFD simulations including fluid-structure interaction (FSI) are capable of providing both. Thus,
52 Gortsas et al. used data made available by the authors of the present paper.

53 There are few studies on the modelling of aeroacoustic low-frequency emission from wind turbines. In the 1980s the NASA
54 developed a code for predicting low-frequency wind turbine noise based on Lawson's acoustic equation applied on rotor forces
55 (Viterna, 1981). Madsen (2010) presented a Blade Element Momentum (BEM) based investigation of low-frequency noise that
56 uses the same theory for the aeroacoustic model. CFD simulations combined with the FW-H propagation method have been
57 applied by Ghasemian and Nejat (2015) and Bozorgi et al. (2018) to assess low-frequency noise of wind turbine rotors. While
58 Madsen considers the influence of the tower on the rotor aerodynamics, Ghasemian and Nejat and Bozorgi et al. study the

isolated rotor. Yauwenas et al. (2017) investigated the blade-passage noise of a generic model turbine numerically using CFD and Curle's acoustic analogy. They found a significant contribution of the induced pressure fluctuations on the tower to the tonal blade-passage noise which was validated with experimental measurements.

In recent years, CFD based fluid-structure coupling has been applied frequently for the investigation of wind turbines. Li et al. (2017) presented a framework of a wind turbine aero-servo-elastic simulation including flexible blades and tower which allows motion of all turbine components. ~~In his approach, controllers for torque and blade pitch are included as well and he focuses his studies on the impact of FSI on aerodynamic rotor loads, drive train dynamics, controllers and wake.~~ **R2:AC8** In their approach, controllers for torque and blade pitch are included as well and they focus their studies on the impact of FSI on aerodynamic rotor loads, drive train dynamics, controllers and wake. Streiner et al. (2008) developed a coupling of the CFD code *FLOWer* to the multibody solver (MBS) *SIMPACK* with the capability to couple isolated wind turbine rotors.

1.3 **R2:C1-c** Scope and objectives

A totally ~~new~~ **R2:AC9** ~~revised~~ *FLOWer-SIMPACK* coupling is revealed in the present paper with the potential to take into account more degrees of freedom, like tower deformation or changes in rotational speed in the structural model and their impact on aerodynamics and aeroacoustics, respectively. Together with the already existing process chain, fully coupled CFD simulations under realistic turbulent inflow conditions can be conducted, providing both airborne and structure-borne emissions simultaneously. A FW-H in-house code is applied to calculate aeroacoustic immission at distant observers while tower base loads represent the structure-borne emission. The aim of the present paper is to identify the sources of low-frequency emissions and to investigate the impact of the complexity of the numerical model on the calculated low-frequency emissions from a generic 5 MW wind turbine. The complexity of the model ~~was~~ **R2:C4** ~~is~~ increased from a rotor only simulation with uniform inflow to a coupled simulation including blade, tower and foundation dynamics with turbulent atmospheric boundary layer. The spectra of tower base loads and acoustic immissions for overall 7 cases ~~were~~ **R2:C4-a** ~~are~~ compared in a frequency range from 0.1 to 25 Hz for evaluation.

2 Numerical process chain

A high fidelity process chain based on multiple solvers was established for the investigation of low-frequency emissions from wind turbines. It consists of the CFD solver *FLOWer*, the MBS solver *SIMPACK* and the FW-H solver *ACCO*. A ~~strong~~ **R2:AC10** coupling between *FLOWer* and *SIMPACK* was developed to generate high fidelity time series of surface pressure distribution on the turbine and structural loads (forces and moments) acting on the foundation of the turbine. Using the CFD results, the aeroacoustic signal at distant, predefined observer positions is computed by means of *ACCO*.

2.1 CFD solver

FLOWer is a compressible, dual time stepping, block structured Reynolds-averaged Navier-Stokes (RANS) solver developed by German Aerospace Center (DLR) (Kroll et al., 2000). The usage of independent grids for bodies and background is enabled

90 by the overlapping grid technique *CHIMERA*, one of *FLOWer*'s main features. The solver is continuously extended at Institute
91 of Aerodynamic and Gas Dynamics (IAG) regarding functionality and performance, including, amongst others, the higher order
92 finite difference weighted essentially non-oscillatory (WENO) scheme (Kowarsch et al., 2013), Dirichlet boundary condition
93 to apply arbitrary unsteady inflow, a body forces approach to superimpose turbulence (Schulz et al., 2016b) and various DES
94 schemes (Weihing et al., 2016). The capability of *FLOWer* for wind turbine simulations has been shown in several projects.
95 The interaction of a wind turbine in complex terrain with atmospheric turbulence was investigated by Schulz et al. (2016a) and
96 code to code comparisons were recently conducted in the European *AVATAR* project (Scheppers et al., 2016).
97

98 **2.2 Multibody solver**

99 *SIMPACK* is a commercial non-linear MBS solver that can be applied to simulate dynamic systems consisting of rigid and
100 flexible bodies. Flexible turbine components like tower and blades are modeled with linear or nonlinear beam theory. The
101 kinematics between the components are defined by joint elements and internal forces can be considered. There are two ways to
102 apply external forces such as aerodynamic forces, either by built-in interfaces or by programmable user routines. Controllers
103 can also be integrated. *SIMPACK* is R2:AC11 has been recently applied by industry and research groups for the simulation
104 of wind turbines, examples can be found in (Luhmann et al., 2017; Jassmann et al., 2014).

105 **2.3 Fluid-structure interaction**

106 To take the influence of unsteady structural deformation on the aerodynamics into account, a coupling between *FLOWer* and
107 *SIMPACK* was implemented. The new approach generally allows coupling of slender beam like structures and is not limited to
108 rotor blades or even wind turbines. Combined coupling of rotating and non-rotating parts can be applied and the deformation of
109 adjacent structures is considered. Furthermore, coupling is not restricted to flexible deformations but also rigid body motions
110 (rotations and translations) can be realized. In the application of wind turbines e.g. pitch motions and changes in rotational
111 speed of the rotor can be transferred from the MBS solver to the CFD solver.

112 For the technical realization, an existing interface that was developed to couple *SIMPACK* with the fluid solver *ANSYS CFX*
113 for the investigation of a tidal current turbine (Arnold et al., 2013) was extended. Furthermore, libraries for grid deformation
114 and load integration which were recently developed and integrated into *FLOWer* (Schuff et al., 2014; Kranzinger et al., 2016)
115 had to be extended for the coupling with *SIMPACK*. Besides the functionality, the main target of the implementation was to
116 keep the set-up of the coupling simple and the dependencies between MBS and CFD models low. Thus, resolution of CFD and
117 MBS model are independent of each other which allows a fast and easy adjustment and replacement of MBS structures or CFD
118 meshes. Furthermore, the new coupling can be restarted, allowing much longer simulation times if *FLOWer* runs on clusters
119 with limited job duration. It was already successfully applied on the blade of a generic 10MW turbine for comparison reasons
120 by Sayed et al. (2016) who implemented a coupling of *FLOWer* to the structural dynamics solver *Carat++*.

2.3.1 General functionality

121

The developed coupling is a partitioned approach, where two independent solvers run simultaneously on different machines and exchange data via Secure Shell (SSH) connection at discrete positions, so called markers. The markers are positioned inside the bodies. While rigid bodies have only one marker, flexible bodies like rotor blades have several markers that are distributed along the beam. On the one hand, deflections and rotations of these markers relative to their non-deformed position are computed by *SIMPACK*. On the other hand, aerodynamic forces and moments acting on these markers are calculated in *FLOWer*. For each structure that is coupled, a communication coordinate system is defined that has to be in the same position and same orientation in both models at all times. It does not have to be fixed, but can be rotating or translating in a predefined way. All data concerning the respective structure is communicated in this coordinate system.

122
123
124
125
126
127
128
129

2.3.2 Mesh deformation

130

The task of the deformation library implemented in *FLOWer* is to apply the deformations of the markers on the corresponding CFD surfaces and to deform the surrounding volume mesh accordingly. The surface is represented by a point cloud which is generated from the CFD mesh. For rigid structures only one marker is used and all surface cloud points perform a rigid body motion based on the translation and rotation of this marker. A cubic spline interpolation is applied for the mapping of flexible structures (beams) consisting of more than one marker. The deformation of each surface cloud point is then realized as rigid body motion based on the corresponding positions along the beam. While a complete spline approach is used for the deflections, taking the rotation at the end points into account, the rotations and the non-deformed marker positions are interpolated using natural splines. A similar approach has been presented by Arnold et al. (2013). ~~Figure 1 shows the surface grid deformation for the first bending mode in a simple test case with 3 markers. Spline interpolation gives a much smoother result in comparison to linear interpolation and considers the non-rotated lower end.~~ Finally, the volume grids are deformed based on the deformation of the point cloud using radial basis functions. To ensure correct overlapping of deformed meshes, holes associated to the deformed surface can also be deformed.

131

132

133

134

135

136

137

138

139

140

141

142

~~Figure 1: Undeformed (black) and deformed (grey) surface mesh, linear interpolation (left) and spline interpolation (right) for a simple test case with three markers. Generic deformation of first bending mode. Rotation at lower end is zero.~~

143

144

2.3.3 Load integration

145

The load library implemented in *FLOWer* enables the calculation of aerodynamic loads on grid surfaces by integration of friction and pressure over the cell faces. ~~For the coupling to *SIMPACK*, the CFD surface is divided into segments based on the deformed marker positions. Loads are integrated for these segments and assigned to the respective markers.~~ This is also necessary for the coupling to *SIMPACK*, as there is no surface in the structural model and the aerodynamic forces have to be mapped to the discrete marker positions. For this purpose, the CFD surface is divided into segments based on the deformed marker positions. For each of these segments, loads are integrated and afterwards assigned to the respective markers. Moments

146

147

148

149

150

151

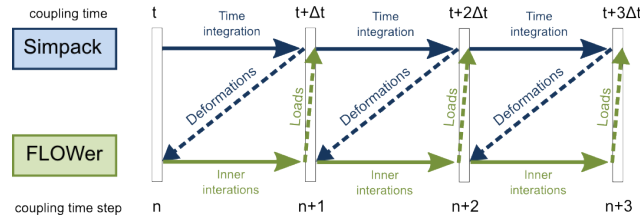


Figure 1. Explicit coupling scheme of the *FLOWer-SIMPACK* coupling.

152 are calculated with respect to the origin of the corresponding communication coordinate system. For structures with only one
 153 marker, loads are integrated over the whole CFD surface of the respective structure.

154 2.3.4 Communication interface

155 The communication is realized by means of files. Data files contain deformations or loads and status files indicate that the
 156 data file is ready to be read. While *SIMPACK* is running on a local Windows machine, *FLOWer* is usually executed in parallel
 157 mode on a high performance computing (HPC) system running on Linux. A portable communication script in Windows in-
 158 herent scripting language PowerShell enables fast and reliable communication between the two solvers. The Linux machine is
 159 accessed using a SSH connection via the Windows Secure Copy (WinSCP) client.

160 2.3.5 Coupling scheme

161 In the presented work, an explicit coupling scheme ~~was~~ **R2:C4-b** ~~is~~ applied. The size of the coupling time step is equal to
 162 the physical *FLOWer* time step and remains constant throughout the simulation. Both solvers are running in a sequential way,
 163 waiting for the other solver to reach the next time step and to send communication data. *SIMPACK* is running one time step
 164 ahead doing time integration with the aerodynamic loads that *FLOWer* computed at the end of the previous time step (Figure 1).
 165

166 2.4 Acoustic solver

167 Acoustic immission at arbitrary observer locations ~~was~~ **R2:C4-c** ~~is~~ calculated by means of the in-house FW-H solver *ACCO*.
 168 Pressure and velocities on surfaces enclosing the noise sources are evaluated at each time step of the transient CFD solution,
 169 including velocities due to deformation, translation and rotation. For the present study, the surfaces used for the acoustic anal-
 170 ysis ~~were~~ **R2:C4-d** ~~are~~ identical with the physical surfaces of the turbine (rotor, tower, hub etc.). Volume sources generated
 171 by free-flow turbulence ~~were~~ **R2:C4-e** ~~are~~ neglected, which is justified for low mach number flow because quadrupole vol-
 172 ume noise is proportional to Ma^7 . This approach was validated for a rod-cylinder configuration and an airfoil in turbulent
 173 flow (Lutz et al., 2015; Illg et al., 2015). The acoustic monopole and dipole contributions to the observer sound pressure level
 174 (SPL) are computed by means of the Ffowcs Williams-Hawkings (FW-H) equation. Its left-hand side is the wave equation
 175 which describes the transmission of sound to the observer, presuming undisturbed propagation and observers located in the

acoustic far field. Hence, ground reflections and non-linear propagation due to atmospheric layering and turbulence are not taken into account. The acoustic far field is defined by the presence of a fully developed wave front and thus starts several wave lengths away from the source. Parallel execution of *ACCO* allows the computation of noise carpets consisting of several thousand observer locations.

The application of the FW-H analogy allows evaluation of the contribution of selected components of the wind turbine to SPL by excluding surfaces of particular components (e.g. tower) from the analysis.

2.5 Computational set-up

2.5.1 The turbine

The examined turbine is based on the NREL 5 MW turbine (Jonkman et al., 2009) and was slightly modified in the *OFFWINDTECH* project (Bekiropoulos et al., 2013). The main modifications concern the rated conditions which were changed to a rotational speed of 11.7RPM and a pitch angle of -2.29° at a wind speed at hub height of 11.3ms^{-1} . The turbine ~~was~~ **R2:C4-f** **is** investigated at rated conditions in an onshore configuration with a hub height of 90m, a rotor diameter of 126m with a tilt angle of 5° and a precone angle of 2.5° . The original tower with a bottom diameter of 6m and a top diameter of 3.87m ~~was~~ **R2:C4-g** **is** used.

2.5.2 CFD model

The CFD model of the *OFFWINDTECH* turbine consists of ten independent body meshes, that are embedded in a Cartesian hanging grid node background mesh using the *CHIMERA* technique. Blades, hub, nacelle and tower ~~were~~ **R2:C4-h** **are** considered in the simulation with fully resolved boundary layer ($y^+ \leq 1$). No gaps are left between the components of the turbine, as blade-hub connectors and a hub-nacelle connector are included in the CFD mesh (Figure 2). Blades ~~were~~ **R2:C4-i** **are** meshed in a C-H-mesh topology with 120 cells in radial direction and 180 cells around the airfoil, summing up to approximately 5.3 million cells per blade. Two different Cartesian background grids ~~were created using hanging grid nodes~~ **R2:C4-j** **with hanging grid nodes are used**. One for the case with prescribed atmospheric turbulence where the mesh is additionally refined to a cell size of 1m^3 upstream of the turbine (64.5 million cells) and another for the case without atmospheric turbulence where only the mesh close to the turbine is refined (20.8 million cells). The computational domain is approximately 48.8 rotor radii (R) long ($12.7R$ upstream of the rotor plane), approximately $24.4R$ wide and has a height of approximately $16.2R$. According to a previous study using *FLOWer* (Sayed et al., 2015), the background grids ~~were expanded~~ **R2:C4-k** **expand** more than sufficient in all directions to avoid influence on the flow field around the turbine. Overall the two set-ups consist of 86 million (fine) respectively 42 million cells (coarse).

Concerning inflow three different cases are regarded in the present study. Uniform inflow, steady atmospheric boundary layer and turbulent atmospheric boundary layer. An exponent of 0.19 ~~was~~ **R2:C4-l** **is** applied for the power law profile describing the steady atmospheric boundary layer, keeping the wind speed at hub height at 11.3ms^{-1} . Atmospheric turbulence with a reference length scale of 42m ~~was created using~~ **R2:C4-m** **, created using** Mann's model (Mann, 1994) ~~and~~ **R2:C4-n** **, is**

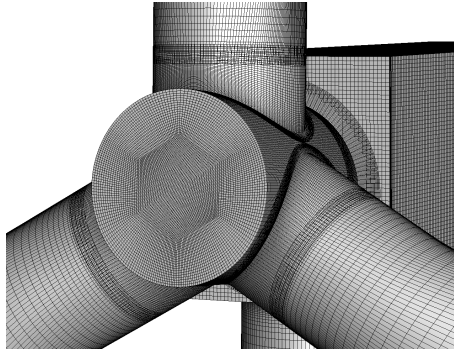


Figure 2. CFD surface mesh, showing the connection of hub, blades and nacelle with overlapping meshes.

208 introduced into the flow field using body forces 16 m downstream of the inlet, superimposing the steady boundary layer profile.
 209 The resulting turbulence level at the turbine position ~~was~~ **R2:C4-o** ~~is~~ 16%. Unsteady RANS (URANS) simulations ~~were~~
 210 **R2:C4-p** ~~are~~ applied with a second order dual time stepping scheme for temporal discretisation. The second order central dis-
 211 cretisation with the Jameson-Schmidt-Turkel (JST) artificial dissipation term ~~was~~ **R2:C4-q** ~~is~~ used for spatial discretisation
 212 in body meshes and fifth order WENO scheme ~~was~~ **R2:C4-r** ~~is~~ applied on the background mesh in order to reduce dissipation
 213 of vortices. Menter-SST (Menter, 1994) was deployed for turbulence modelling. A physical time step corresponding to 0.75°
 214 azimuth ($\approx 0.0168\text{s}$) **Authors** ($\approx 0.01068\text{s}$) with 100 inner iterations ~~was~~ **R2:C4-s** ~~is~~ applied for the evaluated part of the
 215 simulations.

216 2.5.3 Structural model

217 The *SIMPACK* model of the *OFFWINDTECH* turbine was built by Matha et al. (2010). The blades are modelled non-linear
 218 by using multiple flexible bodies per blade. The structural properties of the tower are adopted from the NREL 5 MW turbine
 219 (Jonkman et al., 2009) taking 20 modes into account. Hub and nacelle are defined as rigid bodies. The foundation is modelled
 220 as rigid body connected to the ground with a spring-damper system. ~~Detail~~ **R2:AC13** ~~Details~~ can be found in Table 1.

221 2.5.4 FSI setup

222 ~~The coupling between FLOWer and SIMPACK for the OFFWINDTECH turbine was applied using 160 markers~~ **R2:AC14-a**
 223 **160 markers are used for the fluid structure coupling of the OFFWINDTECH turbine** (Figure 3), 49 markers for each blade,
 224 11 markers for the tower, and nacelle and hub with one marker each. Since in the structural model and the CFD model a fixed
 225 rotational speed ~~was~~ **R2:AC14-b** ~~is~~ prescribed, a rotating communication coordinate system in the center of the hub ~~was~~
 226 **R2:AC14-c** ~~is~~ used for the rotating parts. The communication for tower and nacelle ~~was~~ **R2:AC14-d** ~~is~~ performed in a fixed
 227 coordinate system placed at the tower base (Figure 3). In the *SIMPACK* model of the turbine, additional rigid bodies ~~were~~
 228 **R2:AC14-e** ~~are~~ created for the definition of the undeformed markers. The corresponding moving markers ~~were~~ **R2:AC4-f**
 229 ~~are~~ attached to the flexible structures of the turbine. With this approach the measured deformations between deformed and

Table 1. Details on the foundation of the wind turbine, similar to Gortsas et al. (2017).

Mass	1.888e6 kg
Inertia x, y	82.705e6 kgm ²
Inertia z	88.529e6 kgm ²
Stiffness x, y	8.554e9 Nm ⁻¹
Stiffness z	7.332e9 Nm ⁻¹
Rotational stiffness x, y	559e9 Nm · rad ⁻¹
Rotational stiffness z	559e9 Nm · rad ⁻¹
Damping x, y	240e6 Nsm ⁻¹
Damping z	325e6 Nsm ⁻¹
Rotational damping x, y	5.035e9 Nms · rad ⁻¹
Rotational damping z	4.180e9 Nms · rad ⁻¹

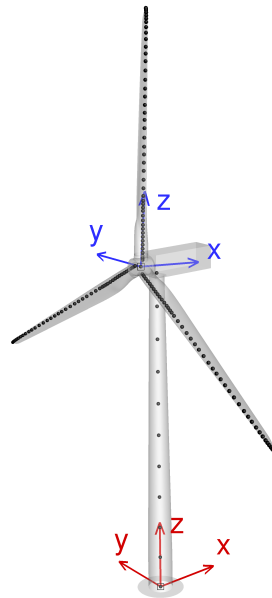


Figure 3. CFD surface of turbine including markers for coupling with *SIMPACK*. Rotating hub coordinate system is shown in blue and tower base coordinate system in red.

undeformed markers are composed of flexible deformations of the body itself plus rigid body motion due to deformation or motion of the adjacent body.

230
231
232

Table 2. Definition of simulation cases, ordered with increasing complexity.

Case name	Inflow	CFD structures	Flexible structures	Background mesh
LC1	uniform	rotor	none	coarse
LC2	uniform	rotor, nacelle, tower	none	coarse
LC2_FSC1SD	uniform	rotor, nacelle, tower	rotor blades SD	coarse
LC2_FSC1	uniform	rotor, nacelle, tower	rotor blades	coarse
LC2_FSC3	uniform	rotor, nacelle, tower	rotor, nacelle, R2:AC12-a rotor blades, tower, foundation	coarse
LC3_FSC3	steady ABL	rotor, nacelle, tower	rotor, nacelle, R2:AC12-b rotor blades, tower, foundation	fine
LC4_FSC3	turbulent ABL	rotor, nacelle, tower	rotor, nacelle, R2:AC12-c rotor blades, tower, foundation	fine

ABL, atmospheric boundary layer; SD, steady deformation.

233 2.5.5 Simulation cases

234 In Table 2 all regarded simulation cases are listed. ~~Three studies were conducted~~ **Authors** ~~For evaluation they are assigned~~
235 ~~to three studies~~. In the first study, no FSI ~~was~~ **R2:C4-t** ~~is~~ considered and thus all turbine components ~~were~~ **R2:C4-u**
236 ~~are~~ kept rigid. The influences of the presence of the tower and the distance of the blade to the tower ~~were~~ **R2:C4-v** ~~are~~
237 evaluated at uniform inflow conditions by comparing LC1, LC2 and LC2_FSC1SD. In case LC2_FSC1SD the ~~averaged blade~~
238 ~~deformations of case LC2_FSC1 were used to create~~ **Authors** ~~blade deformation is equal to the averaged blade deformation~~
239 ~~of case LC2_FSC1 to obtain~~ a realistically deformed shape of the blades with reduced distance between blades and tower. In a
240 second study the degrees of freedom of the structural model ~~were~~ **R2:C4-w** ~~are~~ increased at uniform inflow conditions. Three
241 cases ~~were~~ **R2:C4-x** ~~are~~ compared: a rigid case with steady deformed blades (LC2_FSC1SD), a case with flexible blades
242 (LC2_FSC1) and a case with flexible blades as well as a flexible tower and foundation (LC2_FSC3). In the third study, the
243 inflow conditions ~~were changed~~ **R2:C4-y** ~~are~~ **Authors** ~~varied~~, keeping the structural model the same. Case LC2_FSC3 is
244 used as reference. A steady atmospheric boundary layer (ABL) ~~was~~ **R2:C4-z** ~~is~~ prescribed at the inlet by means of a power
245 law inflow profile in case LC3_FSC3. This steady ABL ~~was~~ **R2:C4-aa** ~~is~~ superposed with velocity fluctuations modelling a
246 turbulent atmospheric boundary layer in case LC4_FSC3.

247 2.5.6 Computational approach

248 ~~One feature of the implemented coupling is that coupled simulations can be started from results of standalone CFD simulations.~~
249 ~~This was applied in the presented research to achieve a well converged state concerning aerodynamic forces and flow field. At~~
250 ~~the same time computational costs could be saved, as coupled simulations with various degrees of freedom could be started~~
251 ~~from the same converged state. In all cases at least 32 revolutions were simulated before the start of the coupling. This was~~
252 ~~necessary due to the high induction of the rotor. The structural simulation is started from a initialized state at the beginning of~~
253 ~~the coupling. All flexible components are released from a rigid state and due to the sudden impact of gravitational, centrifugal~~

and aerodynamic forces, deformations tend to overshoot. As the CFD part of the coupled simulations is computationally expensive, it is important to have a fast convergence of deformations and loads to a periodic state. While flap-wise deflections of the blades are damped very fast, blade edge-wise deflections and tower deflections are not. *SIMPACK* allows the user to define time depended functions for external forces and dampers. As a first step, to reduce deformation velocity at the start of the coupling, aerodynamic loads are multiplied with a linearly increasing load factor over the first 120 time steps (≈ 1.71 s). Additionally, dampers in form of counter acting forces proportional to deformation velocity are attached to the tower tip as well as to the blades to damp initial oscillations of blades and tower. The damping factors are linearly increased and decreased over time and were determined manually for optimal performance of the model. Figure ?? exemplarily shows the force of the tower tip damper in x -direction and the deflection of the tower tip for case LC2_FSC3. The tower damping factor decreases to zero after 740 time steps (≈ 7.91 s). The tower tip deflection shows only a small overshoot and is well converged when the damper is switched off. With this approach, a fast convergence of deflections and loads was achieved and only the first two coupled revolutions of the turbine could not be used for evaluation. **R2:C1-e**

2.6 Evaluation

The aim of the simulation chain is to model airborne and structure-borne emissions simultaneously by evaluating acoustic immission at distant observers and load fluctuations at the tower base. In the fluid-structure coupled simulations tower base loads were **R2:C4-ab** are evaluated directly in the structural model at the interface between tower and foundation, whereas in the non-coupled simulations aerodynamic loads were **R2:C4-ac** are computed from CFD results. In both cases the tower base loads are presented with respect to the tower base coordinate system which is shown in Figure 3. The temporal resolution of the data is equal to the coupling time step. To achieve the same temporal resolution in the acoustic emission, each time step a CFD surface solution was **R2:C4-ad** is saved **R1:Mi5-b** temporarily as input for the acoustic simulations. Acoustic simulations using *ACCO* were **R2:C4-ae** are conducted to calculate the immission at a carpet of observers on the ground surrounding the turbine. Figure 4 shows the 3600 observers located on 20 concentric rings around the turbine at radial positions of 100m to 2000m with a radial resolution of 100m and a circumferential resolution of 2° . Unweighted SPL was **R2:C4-af** is calculated from sound pressure time series at the observers with a reference sound pressure of $20\mu\text{Pa}$. The sound propagation and directivity for discrete frequencies can be evaluated by plotting the SPL contour on the ground. Four observers at a distance of 1000m to the turbine were **R2:C4-ag** are chosen for detailed evaluation of SPL spectra (large dots in Figure 4). Prior to frequency analyses by means of fast Fourier transform (FFT), the time series signals of loads and sound pressure were **R2:C4-ah** are cut to multiples of one rotational period of the turbine in order to supply a preferably periodical signal to the FFT and to avoid influence of start-up effects. In coupled simulations, the first two revolutions were **R2:C4-ai** are excluded from evaluation. For case LC4_FSC3 14 revolutions and for all other cases 8 revolutions were **R2:C4-aj** are evaluated. **R1:Mi5-a** As the sampling rate is equal to the physical time step of the simulation, the highest resolved frequency (Nyquist frequency) is 46.8 Hz.

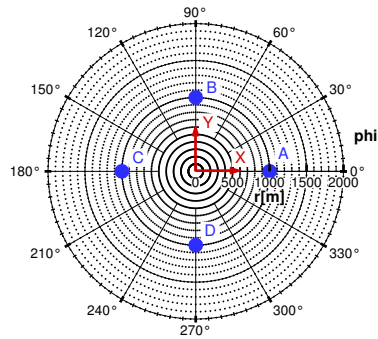


Figure 4. Observer positions for evaluation of aero acoustic emissions. Tower base coordinate system shown in red. View from above, turbine in the center, wind from left.

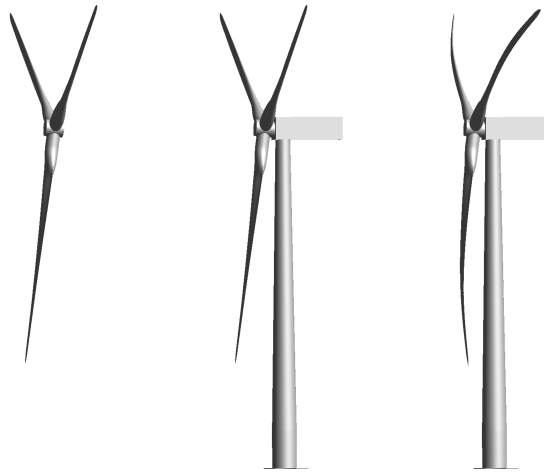


Figure 5. CFD turbine surfaces of cases LC1 (left), LC2 (middle) and LC2_FSC1SD (right). Snapshot with one blade in front of the tower at 180° azimuth.

286 3 Results

287 3.1 Rigid simulations

288 In this section three non-fluid-structure coupled cases are compared at uniform inflow conditions. As reference the rotor only
 289 case (LC1) is regarded where unsteady effects on the loads only result from the tilt of the rotor, the proximity to the ground
 290 and unsteady flow separation. In a second case, the tower is considered (LC2) and in a third case steady deformation is applied
 291 to the blades (LC2_FSC1SD). The CFD surfaces of all three cases are shown in Figure 5.

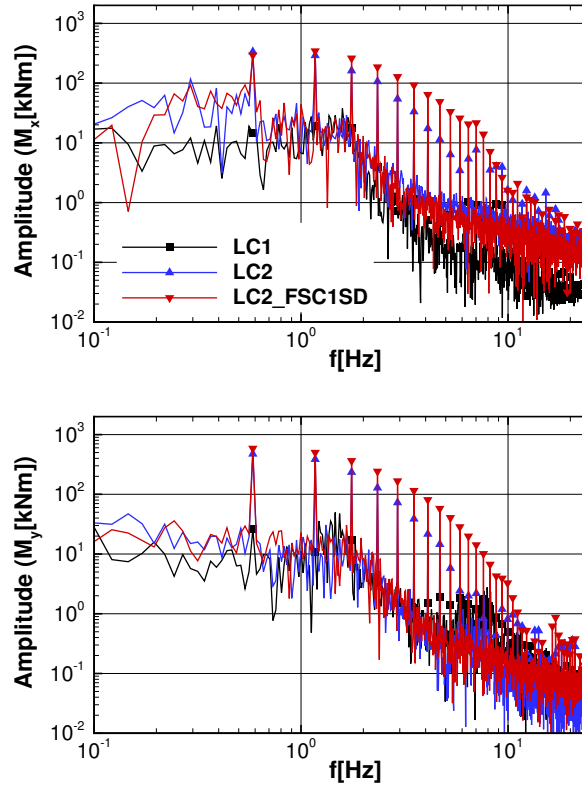


Figure 6. Spectra of tower base loads ~~R2:AC17-b~~ aerodynamic loads with respect to tower base (moment reference point) for cases LC1, LC2 and LC2_FSC1SD. ~~R2:C3-c~~

3.1.1 Tower base loads

292

In the non-fluid-structure coupled cases no unsteady structural forces occur as all structures are rigid. Thus, load fluctuation 293 only arise from aerodynamics. Figure 6 shows the spectra of the aerodynamic loads ~~R2:C3-d~~ M_x and M_y of all three cases 294 with respect to the tower base coordinate system ~~R2:AC17-a~~ (moment reference point). No distinctive peaks can be found 295 in the spectra of LC1. After including the tower in the simulation (LC2), sharp peaks at the blade-passing frequency and its 296 higher harmonics appear with significantly increased amplitudes up to a frequency of approximately 10 Hz. Regarding F_y and ~~R2:C3-e~~ M_x , a general increase of the amplitudes below BPF are ~~R2:C3-f~~ is present with a peak at approximately 0.3 Hz 298 caused by vortex shedding, which will be shown later. In LC2_FSC2SD the distance between tower and blades is reduced due 299 to the steady deformation of the blades. This leads to an increase of the amplitudes at blade-passing harmonics. The relative 300 increase is stronger for higher frequencies. The amplitude of F_x ~~R2:C3-g~~ M_y is increased by more than 50% for frequencies 301 between 5 Hz and 10 Hz. For F_y and ~~R2:C3-h~~ M_x the amplitude at BPF stays almost constant while amplitudes are increased 302 for the higher harmonics compared to case LC2. The maximum amplitude of M_x is shifted to the second harmonic of BPF. 303

304 The amplitudes of F_z and M_z are much lower compared to the other load components **R2:C3-i** M_z are much lower compared
305 to the other load components and therefore are not shown.

306 The composition of the **R2:AC18-a** aerodynamic loads was investigated in detail for case LC2_FSC1SD. Therefore, aerody-
307 namic loads on rotor and tower were evaluated separately **R2:AC18-b** with respect to tower base coordinate system (moment
308 reference point). Figure 7 shows the resulting spectra. ~~For all loads except F_z and M_z , the~~ **R2:C3-j** The peak amplitudes of
309 the tower spectra are dominant over the whole frequency range. Especially for F_y and **R2:C3-k** M_x the tower load amplitudes
310 are up to ten times higher compared to the rotor load amplitudes. For F_y and **R2:C3-l** M_x the general level below BPF is
311 higher in the tower load spectra. This can be interpreted as the impact of unsteady flow separation at the tower induced by
312 vortex shedding. This phenomenon, known as von Kármán vortex street, leads to unsteady forces on blunt bodies with a fre-
313 quency described by the dimensionless Strouhal number. ~~Assuming a Strouhal number of 0.2 and an inflow velocity of 8ms^{-1}~~
314 ~~(reduced due to induction of the rotor), the frequency of the undisturbed vortex shedding should be around 0.32 Hz with respect~~
315 ~~to the mean diameter of the tower of 4.9 m.~~ **R2:AC20** Assuming an inflow velocity of 8ms^{-1} (reduced due to induction of
316 the rotor) results in a Reynolds number of $2.8 \cdot 10^6$ with respect to the mean diameter of the tower (4.9 m). The corresponding
317 Strouhal number of approx. 0.24 leads to a theoretical vortex shedding frequency of 0.38 Hz. As both, diameter and inflow
318 velocity are not constant over the length of the tower and inflow is disturbed by the rotor, a broader range of vortex shedding
319 frequencies can be expected. ~~In Figure 10 the time series of aerodynamic loads F_y and M_x acting on the tower are displayed.~~
320 ~~It is clearly visible that the peaks appearing periodically with the BPF are superimposed with a lower frequency oscillation.~~

321 **R2:C3-m** **R2:AC21** as it is present in the spectrum of M_x .

322 ~~Figure 10~~ **R2:C3-n**

323 The surface pressure amplitudes on the tower are displayed in Figure 8 at two different frequencies. At BPF (0.585 Hz) as well
324 as at 0.292 Hz where the spectra of F_y and **R2:C3-o** M_x have a local maximum. A strong peak appears at BPF at the front
325 of the tower shifted to the side of the approaching blade. The symmetric shape of the pressure amplitude distribution and the
326 higher amplitudes at the rear side of the tower at 0.292 Hz can very likely be associated with vortex shedding creating the peak
327 in the load spectra. These observations support the idea of the superposition of blade-passing effects and vortex shedding at the
328 tower.

329

330 3.1.2 Aeroacoustic emission

331 Figure 9 shows the spectra of the SPL for observers ~~A-D for the cases LC1, LC2 and LC2_FSC1SD.~~ **R2:C3-q** **C** and **D**
332 **for the cases LC1, LC2 and LC2_FSC1SD.** The immission at observer A is very similar to the one at observer C. The same
333 **applies to observers B and D.** The maximum SPL for LC1, the case without tower, occurs at observer B at BPF and is the only
334 prominent peak. The emission at this frequency shows a strong directivity, as the amplitude is much higher at the sides than
335 upstream and downstream of the turbine. The presence of the tower (LC2 and LC2_FSC1SD) causes a massive increase of
336 amplitudes at the BPF harmonics while the broadband noise level stays low. The highest peak appears upstream of the turbine
337 at observer C at the third BPF harmonic and is approx. 4 dB higher in case LC2_FSC1SD compared to case LC2. The spectra

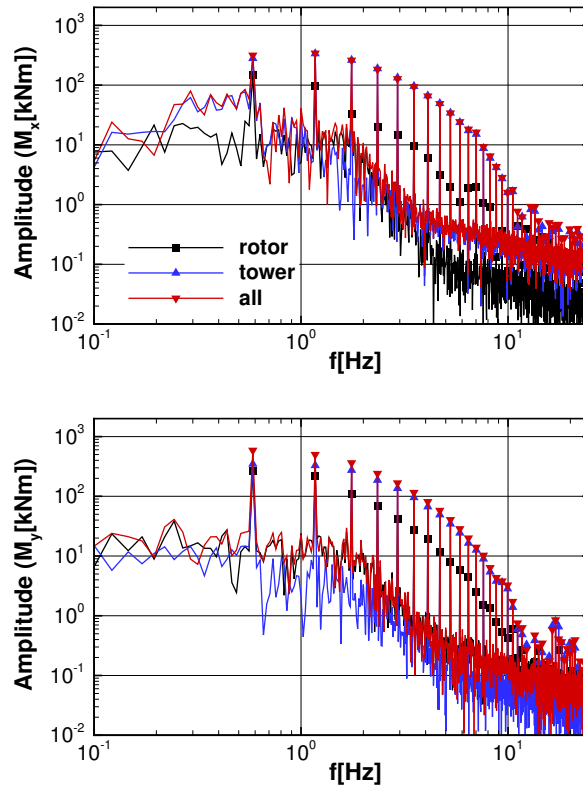


Figure 7. Spectra of tower-base loads R2:AC18-c aerodynamic loads with respect to tower base (moment reference point) for case LC2_FSC1SD. Authors Comparison of loads on rotor, tower and all surfaces. R2:C3-p

of case LC2 show only a weak directivity for the BPF harmonics as the amplitudes at the upstream and downstream observers 338 are just slightly lower than at the side observers. A stronger directivity can be observed for case LC2_FSC1SD at BPF where 339 the amplitudes are clearly higher at the upstream and downstream observer. Compared to case LC1 the SPL at frequencies 340 below BPF also rises, but only at observer positions B and D. Comparing LC2_FSC1SD to LC2, the increase of amplitudes 341 due to reduced blade-tower distance is most prominent between fifth and tenth harmonic of BPF where it amounts to more than 342 10 dB. The SPL peaks drop below 20 dB at around 15 Hz even for case LC2_FSC1SD. 343

To examine the aeroacoustic noise emission in detail, the noise emission originating from tower and rotor surfaces were 344 evaluated separately for case LC2_FSC1SD. Figure 10 shows the SPL spectra at observer positions ~~A-D~~ R2:C3-t C and D. 345 It can be seen that for all BPF harmonics the calculated SPL emitted by the tower is higher than the one emitted by the rotor. 346 The global maximum of the rotor induced immission is about 8 dB lower compared to the global peak of the tower induced 347 immission, both occur at observer C. The emission from the rotor shows a strong directivity to the upstream and downstream 348 direction, with clearly lower amplitudes at observers B and D. At BPF, the emission of the tower shows the same directivity, yet 349

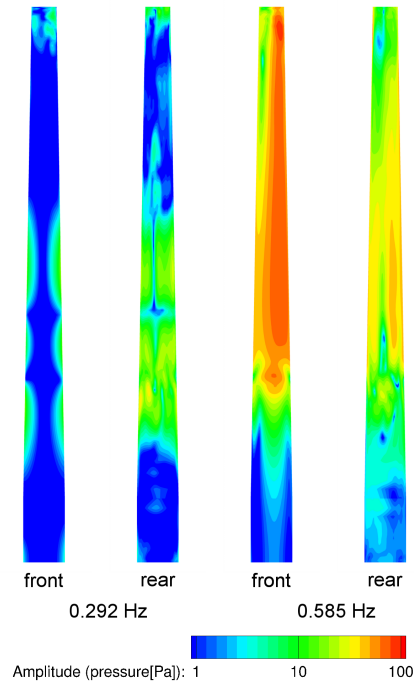


Figure 8. Pressure amplitudes on CFD tower surface of case LC2_FSC1SD at 0.292 Hz (left) and blade-passing frequency (0.585 Hz) (right).

350 less pronounced, whereas the directional differences at higher harmonics of BPF are marginal. The SPL increase in the plane of
 351 rotation for frequencies below BPF is mainly caused by the tower emission. This is similar to the increase of amplitudes in the
 352 tower base load spectra for F_y and M_x caused by pressure fluctuations on the tower surface which was described in
 353 the previous section. Thus SPL increase at frequencies below BPF is very likely induced by surface pressure fluctuations due to
 354 vortex shedding at the tower, too. Looking at the noise carpet for the third BPF harmonic in Figure 11 gives more insight into
 355 the directivity. The rotor emission is strongly directed towards 20° and 190° , whereas for the tower emission only a small shift
 356 of the generally concentric shape towards 220° is present. The superposed signal shows a directivity towards $180^\circ/350^\circ$ and
 357 is slightly biased upstream. The result also shows that the shape of the SPL isolines beyond approx. 500m radius around the
 358 turbine is independent of the radius. The same behaviour can be observed for the other harmonics of BPF. Thus, the previously
 359 regarded observers at 1000m radius are clearly out of near field effects for BPF harmonics.
 360

361 3.2 Influence of degrees of freedom at uniform inflow

362 In the second study the cases LC2_FSC1SD, LC2_FSC1 and LC2_FSC3 are regarded. The aim is to evaluate the influence of
 363 the degrees of freedom of the structural model on the low-frequency emissions from the wind turbine. Case LC2_FSC1SD has

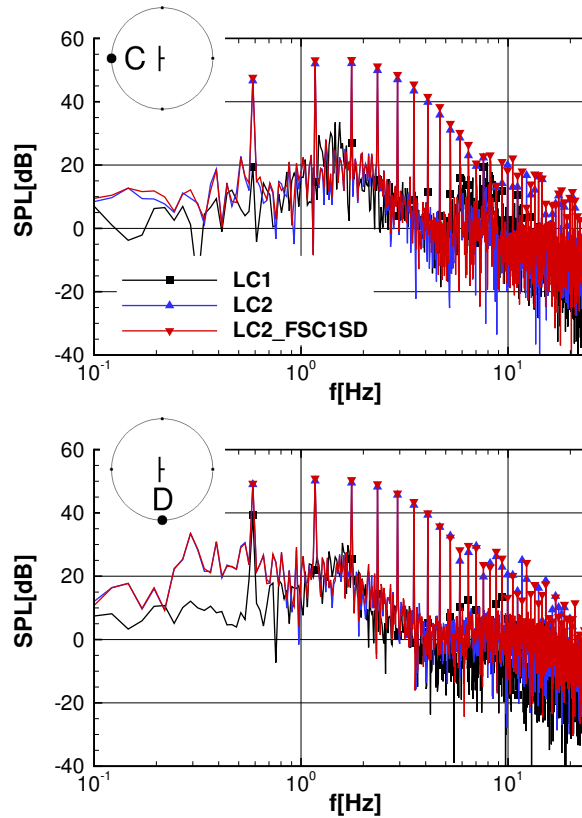


Figure 9. Spectra of unweighted SPL (reference sound pressure of $20\mu\text{Pa}$) at ~~4~~ **R2:C3-r** two observer positions on the ground with a distance of 1000m to the turbine for cases LC1, LC2 and LC2_FSC1SD. **R2:C3-s**

zero degrees of freedom but considers the mean blade deformation of case LC2_FSC1 where only the rotor blades are flexible, 364
 thus it has been chosen as reference case for this study. 365

3.2.1 Tower base loads 366

The spectra of the tower base loads for all three cases are plotted in Figure 12. The flexibility of the rotor blades in case 367
 LC2_FSC1 has mainly an impact on the amplitudes at harmonics of BPF. ~~While the amplitudes in F_x decrease slightly, the~~ 368
~~amplitudes in F_y rather increase. A clear increase of F_z at BPF and some higher harmonics is present.~~ **R2:C3-w** M_x ampli- 369
 tudes ~~also~~ **R2:C3-x** increase with the highest peaks at first and second harmonic of BPF rising by more than 30% compared 370
 to case LC2_FSC1SD. On the contrary a decrease is observed for M_y , especially for the second and third harmonic of BPF. ~~M_z~~ 371
~~stays on a much lower level than M_x and M_y but amplitudes at most higher harmonics of BPF are increased compared to the~~ 372
~~reference case.~~ **R2:C3-y** 373

There are two effects which go hand in hand both having an influence on the tower base loads. By setting the blades flexible, 374

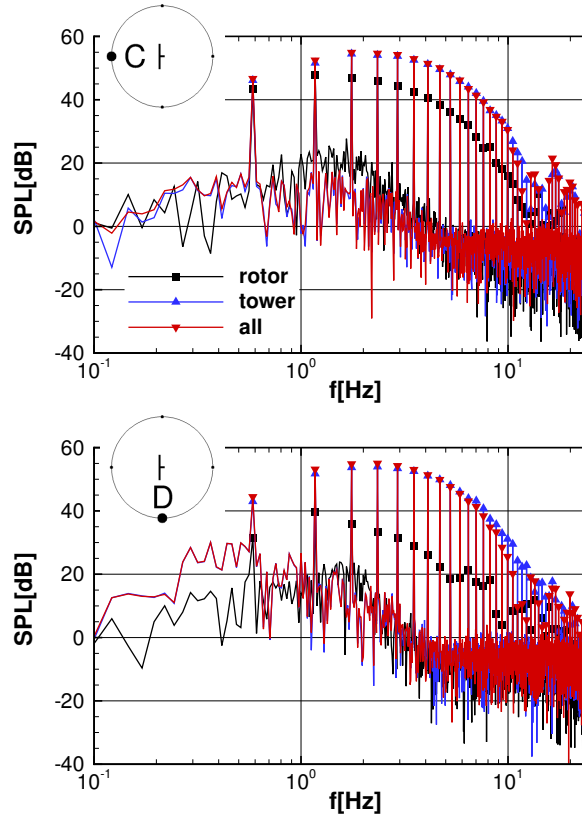


Figure 10. Spectra of unweighted SPL (reference sound pressure of $20\mu\text{Pa}$) at 4 **R2:C3-v** two observer positions on the ground with a distance of 1000m to the turbine for case LC2_FSC1SD. Comparison of **emission- Authors noise emitted** from rotor, tower and all surfaces.

375 on the one hand, gravitational forces and inertial forces start acting and on the other hand, aerodynamic forces change due to
 376 unsteady deflection of the blades. The mean blade tip deflection applied in case LC2_FSC1SD is 6.34m out of plane (OOP)
 377 and -0.58m in plane (IP). In case LC2_FSC1 the OOP deflection reaches its maximum of approximately 6.46m when the
 378 blade is passing the tower, just before the blade deformation is reduced due to the tower blockage. The IP deflection oscillates
 379 between -0.13m and -1.02m , which is mainly caused by the gravitational force that makes the blade bend downwards. Due
 380 to the inertia of the blade, the IP blade tip velocity reaches its maximum just after the tower passage. This increases the abso-
 381 lute velocity of the blade when passing the tower and the relative flow velocity on the blade. On the other hand, the swinging
 382 of the blades mainly induces structural forces in y and z direction which explains the increase of F_y and F_z **R2:C3-aa**
 383 M_x amplitudes at BPF. The enabled flexibility of the tower in case LC2_FSC3 shows a much stronger impact on the tower
 384 base loads compared to case LC2_FSC1 as it significantly changes the structural eigenmodes of the turbine. **Regarding the**
 385 **dominant loads $F_x, F_y,$ **R2:C3-ab** in M_x and M_y , the amplitudes at first, second and third harmonics of BPF are clearly**
 386 **reduced. Especially the reduction at BPF is remarkable, over 70% for **R2:C3-ac** both loads all four load components.** For M_x

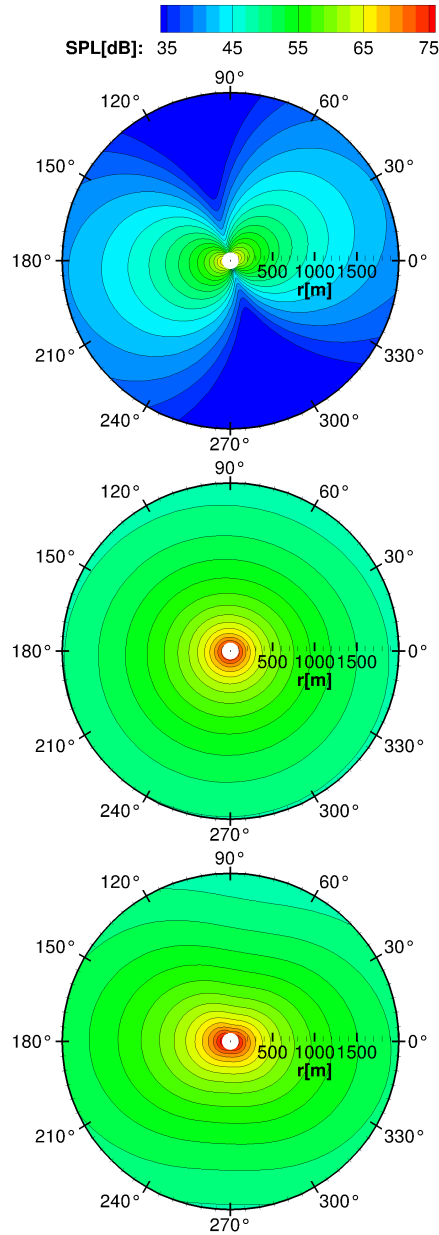


Figure 11. Unweighted SPL (reference sound pressure of $20\mu\text{Pa}$) at third BPF harmonic (1.755 Hz) on ground around the turbine for case LC2_FSC1SD. Aeroacoustic emission from rotor (top), tower (middle) and all surfaces (bottom). ΔSPL between black contour lines is 2 dB.

the amplitude at BPF even drops to the level of the broadband fluctuations of the other two cases. For F_x and **R2:C3-ad** M_y 387
the maximum amplitude shifts to the fifth harmonic of BPF which is close to three structural eigenfrequencies of the turbine. 388
For F_y and **R2:C3-ae** M_x it occurs at approximately 0.32 Hz which matches with the first side-side bending mode of the 389

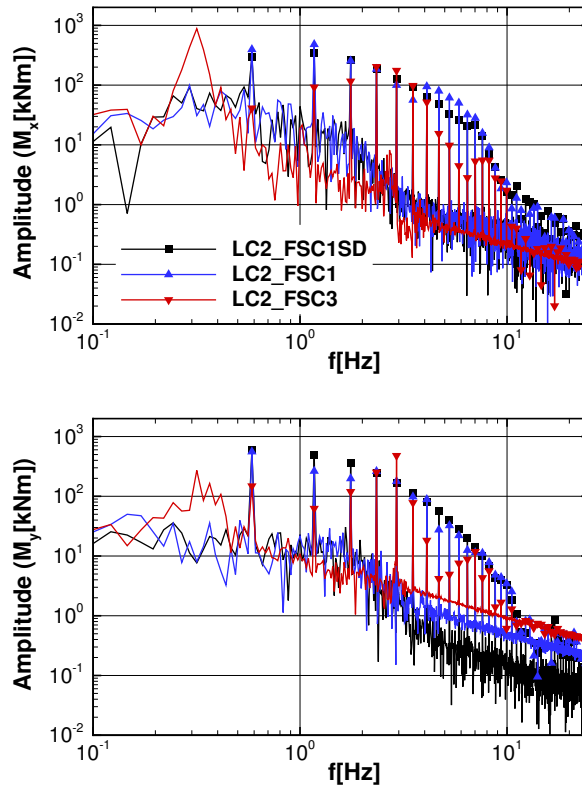


Figure 12. Spectra of ~~tower base loads~~ **R2:C3-z** tower base bending moments for the cases LC2_FSC1SD, LC2_FSC1 and LC2_FSC3.

390 tower. An increase of the amplitudes in the frequency range around 0.32 Hz can also be observed for F_x and **R2:C3-af** M_y ,
 391 yet less pronounced. The first fore-aft bending mode is also at this frequency but the aerodynamic damping is much higher
 392 compared to the side-side direction. ~~For F_z amplitudes at higher harmonics of BPF are increased but the maximum amplitude,~~
 393 ~~occurring at BPF, is reduced. For M_z a further increase of the amplitudes of second to sixth harmonics of BPF is present and~~
 394 ~~the maximum amplitude is increased and shifted to the fifth harmonic of BPF.~~ **R2:C3-ag**

395

396 3.2.2 Aeroacoustic emission

397 The increase of degrees of freedom in the structural model only marginally influences the SPL at the ~~observer positions A-D~~
 398 ~~().~~ The spectra at observer positions A and C show a small decrease of the amplitude at BPF while there is a small increase
 399 at second to sixth harmonics of BPF. However, observers B and D show a small increase at BPF while amplitudes of higher
 400 harmonics are almost unchanged. **R2:C3-ah** observers. The spectrum at observer position C shows a small decrease of the
 401 amplitude at BPF while there is a small increase at second to sixth harmonics of BPF. However, observer D shows a small

increase at BPF while amplitudes of higher harmonics are almost unchanged. Generally, the effect is a bit stronger for case LC2_FSC3. These small changes might be an impact of the slightly reduced blade-tower distance and the increased blade tip velocity when the blade passes the tower which was reported in the previous section. For frequencies below BPF, the maximum amplitude increases slightly which could be induced by the structural eigenmodes of the turbine as well as by the impact of vortex shedding at the tower.

~~Figure 16: Spectra of unweighted SPL (reference sound pressure of 20 μPa) at 4 observer positions on the ground with a distance of 1000 m to the turbine for cases LC2_FSC1SD, LC2_FSC1 and LC2_FSC3.~~ **R2:C3-aj**

3.3 Influence of inflow

In the last study the influence of inflow conditions on the tower base loads and on the aeroacoustic emission is investigated. While uniform inflow was applied for the previous studies, more realistic inflow is considered in this study. Two cases, one with vertically sheared inflow (LC3_FSC3) and one with turbulent vertically sheared inflow (LC4_FSC3) are compared to the uniform inflow case (LC2_FSC3). For the turbulent inflow case a longer time series is evaluated in order to obtain more representative results.

3.3.1 Tower base loads

The spectra of tower base loads in Figure 13 show that for case LC3_FSC3 an increase of amplitudes is only present for F_x , F_z , M_y and M_z and only M_y at BPF. Especially the amplitude of M_z at BPF rises to a remarkably high level. **R2:C3-ak** **R2:C3-al** Amplitudes at higher harmonics of BPF tend to reduce for all loads except for M_z **R2:C3-am** M_x and M_y . The result also shows that the broadband load level at frequencies between first and fifth BPF harmonics rises. For F_y and M_x there is a clear peak just above 1 Hz which even exceeds the peak at BPF **R2:C3-ao** for M_x . The reduction of amplitudes at higher harmonics of BPF can be explained as a result of the reduced inflow velocity below hub height due to the power law profile. Because of the lower aerodynamic thrust in this region, OOP deflection in front of the tower reduces to approximately 5.5 m compared to 6.46 m in case LC2_FSC3. The rise of amplitudes at BPF can be explained as an effect of vertical shear. While blade-passing is a short pulse and many higher harmonics of BPF are excited, the effect of vertical shear stretches over the whole revolution and is much closer to a sine function. Thus, the excitation of higher harmonics of BPF is much weaker compared to blade-passing. The combination of vertical shear and reduced blade-passing effect finally leads to an increase of amplitudes at BPF while amplitudes at higher harmonics decrease.

By superimposing turbulence to the vertically sheared flow in case LC4_FSC3, the character of the spectra changes as the amplitudes at BPF harmonics become much less prominent. There are some clear peaks remaining, but the broadband load level massively increases. The global maximum now arises for M_y at approximately 0.32 Hz corresponding to an eigenmode of the structural model. Additionally the amplitude at BPF is strongly increased for F_x , F_y , M_x and M_y ; however, side peaks occur that are partially even higher. The amplitude at approximately 1 Hz further increases compared to case LC3_FSC3 and another wide peak appears at frequencies around approximately 2.75 Hz, which again corresponds to nearby structural eigenmodes. The higher amplitudes at frequencies near to structural eigenmodes can be explained by the broadband excitation

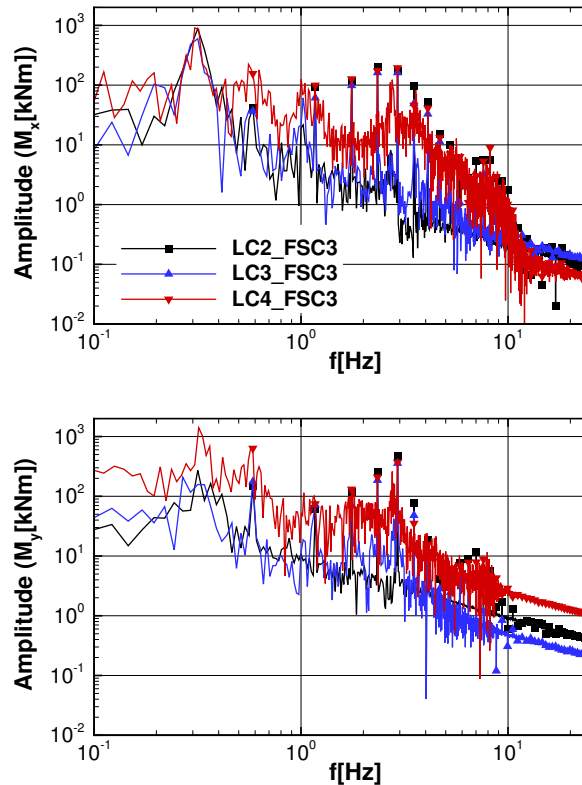


Figure 13. Spectra of tower base loads- R2:C3-ap tower base bending moments for the cases LC2_FSC3, LC3_FSC3 and LC4_FSC3.

435 due to the influence of turbulent inflow on the aerodynamic loads. Without turbulent inflow the main excitation occurs at BPF
 436 harmonics because all unsteady effects except for the vortex shedding are periodic with BPF (blade-tower interaction, tilt angle,
 437 vertical shear).

438 3.3.2 Aeroacoustic emissions

439 Figure 14 shows the spectra of the acoustic immission at observers ~~A to D~~ R2:C3-ar C and D for the regarded cases. The
 440 vertically sheared inflow (case LC3_FSC3) leads to a slight decrease of SPL at BPF harmonics with a stronger effect at higher
 441 frequencies. Only a small increase of amplitude can be observed at BPF for observers ~~B and~~ R2:C3-as D. For observers
 442 ~~A and~~ R2:C3-at C an increase in the broadband noise level between approximately 2 Hz and 10 Hz can be found, but it
 443 does not exceed 30 dB. The reduction of SPL can be explained with the reduced blade tip deflection in front of the tower
 444 already mentioned above, which reduces the pressure fluctuations on the tower. Taking the turbulent inflow into account (case
 445 LC4_FSC3) leads to an increase of the broadband noise level due to turbulent inflow noise, generated by the interaction of
 446 the rotor blade with the turbulence. The inflow noise is emitted from the rotor and predominantly directed in upstream and

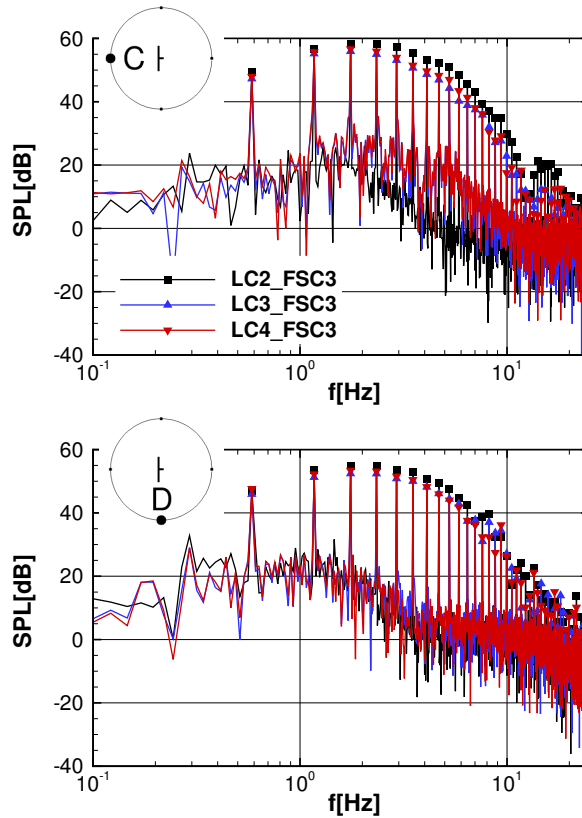


Figure 14. Spectra of unweighted SPL (reference sound pressure of $20\mu\text{Pa}$) at ~~4~~ **R2:C3-ap** ~~two~~ observer positions on the ground with a distance of 1000m to the turbine for cases LC2_FSC3, LC3_FSC3 and LC4_FSC3.

downstream direction, leading to higher broadband noise levels at observers ~~A and~~ **R2:C3-au** C compared to observers ~~B~~ 447
~~and~~ **R2:C3-av** D. Since the rotor blades encounter the turbulence at considerably higher relative velocity than the tower, the 448
emission from the tower hardly increases compared to case LC3_FSC3. However, despite the increased broadband noise level, 449
the peaks at BPF harmonics are still dominant at all four observer positions. 450

4 Discussion 451

In the first study the influence of the presence of the tower and of steady blade deformation on low-frequency emissions was 452
evaluated at uniform inflow conditions in standalone CFD simulations. Concerning the aerodynamic loads, the presence of 453
the tower leads to an increase of amplitudes at BPF and its higher harmonics. Applying a steady deformation to the rotor 454
blades further increases the amplitudes especially for higher harmonics due to the stronger blade-tower interaction. Splitting 455
the loads up into rotor and tower loads shows that the major part of the fluctuations originates from the tower and is caused 456
by blade-tower interaction. Load oscillations induced by vortex shedding can be observed but do not play an important role. 457

458 Evaluating the aeroacoustic immission on the ground at a distance of 1000m shows similar results. Through the presence of the
459 tower a tonal noise emission with prominent peaks at BPF harmonics arises. Reduced blade-tower distance further increases
460 the amplitudes of BPF harmonics especially at higher frequencies. Comparing the contributions of tower and rotor to the noise
461 emission shows a strong directivity for the rotor emission in the direction of the rotor axis and a weak directivity for the tower
462 emission except at BPF. Generally the emission from the tower is stronger in all directions in the regarded frequency range.
463 This corresponds to the findings by Yauwenas et al. (2017) who did research on blade-passage noise and claimed a significant
464 contribution of the tower. While Yauwenas et al. investigated a small model turbine with a symmetric blade in stationary air
465 and a BPF of 45 Hz, the present study shows that their assumption is also valid for a realistic multi megawatt turbine under
466 uniform inflow and a BPF in the low frequency range.

467 In a second study, the influence of degrees of freedom in the structural model was investigated using three cases, one with
468 steady blade deformation already regarded in the first study, another with flexible blades and a third with additionally flexible
469 tower and foundation. Flexible blades have only a minor impact on the calculated tower base loads. Structural eigenmodes
470 play a more significant role in the third case when tower and foundation are flexible too. The peaks at BPF harmonics are still
471 prominent but the amplitudes change and the maxima are shifted towards BPF harmonics close to structural eigenfrequencies.
472 Additionally, peaks corresponding to the first bending modes of the tower (0.32 Hz) occur, being dominant in F_y and M_x
473 spectra **R2:C3-aw** the spectrum of M_x . Concerning aeroacoustics, the emission slightly increases but no clear influence of
474 structural eigenmodes can be found in the regarded frequency range.

475 The third study deals with the influence of the inflow condition on the emissions. Uniform inflow is compared to vertically
476 sheared inflow with and without turbulence. For vertical shear inflow tower base loads tend to increase at BPF and decrease at
477 higher harmonics of BPF. With superimposed turbulence the peaks become much less prominent since the broadband load level
478 rises. Amplitudes at frequencies close to structural eigenmodes rise and BPF harmonics become less dominant in the spectra.
479 The tonal noise level of the aeroacoustic emission tends to reduce slightly with the vertical shear and increase again due to
480 the superimposed turbulence. The broadband noise level strongly increases especially for observers upstream and downstream
481 of the turbine, which is mainly caused by turbulent inflow noise emitted by the rotor. Thus, the BPF harmonics become less
482 prominent but are still dominant in the spectra.

483 As a generic wind turbine was investigated, no measurements for validation are available. Nevertheless, a qualitative com-
484 parison between the presented results and two studies found in literature is drawn. Zieger and Ritter (2018) showed seismic
485 measurements in Germany that suggest an independence of discrete frequency peaks and blade-passing frequency. Although
486 the amplitudes increase with increasing wind speed and rotational speed respectively, the frequencies of the peaks do not
487 change. This can be interpreted as a dominance of structural eigenmodes of the turbine in the origin of the seismic waves.
488 However, at high (rated) rotational speed the dominant frequencies correspond very well to harmonics of the blade-passing
489 frequency. Saccorotti et al. (2011) analyzed seismic measurements of a gravitational wave observatory in Italy close to a wind
490 farm and found steady spectral lines as well as time-varying peaks which could all be identified as emitted by a wind turbine.
491 The results of both studies coincide with the findings of the presented paper where tower base loads at BPF harmonics close to
492 eigenfrequencies of the turbine are prominent in the spectra. The tonal character of the low-frequency noise was also shown in

acoustic field measurements (Hansen et al., 2017; Pilger and Ceranna, 2017). They showed that the BPF harmonics are dominant in the measured spectra and thus the peak frequencies shift depending on the rotational speed of the turbine. Pilger and Ceranna furthermore compared measurements of a single 200 kW turbine to estimated SPL from the Viterna method (Viterna, 1981). They found an underestimation of SPL which they explained with environmental conditions neglected in the model. Taking the present study into account it is more likely that the neglect of tower emission in the Viterna method has a major impact on the results.

Despite the advanced modelling approach applied in the presented study, there are still several limitations that have to be mentioned. In the applied FW-H calculations effects of unsteady flow field, refraction and reflection of acoustic waves and atmospheric layering are not taken into account for the propagation. On the other hand, this makes the method very suitable for the investigation of the aeroacoustic emission of the turbine, as the immission at the observer positions is not influenced by the effects mentioned above. Due to the computationally expensive CFD approach, there are limitations concerning the length of the time series and temporal resolution and consequently the statistical convergence of the results and the resolved frequency range. Although the flexibility of rotor blade, tower and foundation was considered in the simulations further degrees of freedom were neglected. The drive train was kept totally rigid and at fixed rotational speed. As *SIMPACK* is a multibody solver and only deformations of points along a beam are transferred, eigenmodes of the shell cannot be considered in the presented approach. However, the mentioned shortcomings do not change general findings of this paper.

5 Conclusions

In the present paper the low-frequency emissions from a generic 5 MW turbine were investigated using a high fidelity time resolved fluid-structure coupled CFD approach. Three different studies were conducted to identify sources, to better understand mechanisms and to evaluate the influence of the model complexity on the resulting emissions. Tower base loads are compared to study the effect of structure-borne noise as seismic wave propagation cannot be calculated with the presented method. The aeroacoustic noise propagation is computed using a Ffowcs-Williams Hawkins method. To consider aeroelasticity in the simulations a new coupling of the CFD solver *FLOWer* to the MBS solver *SIMPACK* was developed and is presented in this paper. With this method not only blade deformation can be taken into account, but deformations, translations and rotations of all parts of the turbine. Thus, fluid-structure coupled simulations with flexible tower and foundation could be conducted.

~~As a high fidelity approach is used, the aerodynamic results are of high quality.~~ **R2:AC23** A major advantage compared to lower fidelity approaches is that, as all geometries of the turbine are fully resolved, the unsteady pressure distributions on all surfaces, and thus all aerodynamic loads, are a direct outcome of the simulations. Regarding the aeroacoustic emission it was found that the blade-tower interaction plays a key role and the noise emitted from the tower is higher compared to the noise emitted from the rotor. Only an indirect impact of fluid-structure-coupling on the aeroacoustics could be observed. Elastic blades reduce the distance between blade and tower and thus increase the strength of the blade-tower interaction. Turbulent inflow on the other side mainly influences the broadband noise level of the rotor. For the regarded turbulence level of 16% the noise has a tonal character with dominant peaks at blade-passing frequency harmonics.

526 Blade-tower interaction also has a great influence on the tower base loads; however, with increasing degrees of freedom struc-
527 tural eigenmodes play a much stronger role than for the aeroacoustic emission and amplitudes at eigenfrequencies become
528 more dominant when turbulent inflow is applied. Nevertheless, blade-passing frequency harmonics can still be identified in
529 the spectra. For aerodynamic load fluctuations at uniform inflow it was found that the contribution of the tower exceeds the
530 contribution of the rotor.

531 Several conclusions for the modelling of low-frequency emissions using CFD simulations can be drawn from the conducted
532 studies. The blade-tower interaction was found to be the main source of aeroacoustic noise and triggers a major part of the
533 aerodynamic load fluctuations. The tower itself as well as a realistic blade-tower distance has to be considered in the simulation
534 to capture the blade-tower interaction properly. Fluid-structure coupling is the most appropriate way to a realistic blade-tower
535 distance and is mandatory if structural emission shall be regarded. Moreover the acoustic emission from the tower has to be
536 considered in the noise evaluation and the loads on the tower have to be included in the fluid-structure coupling. Concerning the
537 structural emission, not only the flexibility of the rotor blades but also of tower and foundation have to be taken into account
538 as they change the character of the tower base load spectra. Turbulent inflow should also be taken into account, because it
539 enhances the excitation of structural eigenmodes.

540 The findings can be transferred to any modelling method of low-frequency emissions from wind turbines. The method has to
541 be capable of capturing the impact of blade-passing not only on the blades but also on the tower and its effect on the one hand
542 on the aerodynamic load fluctuations and on the other hand on the aeroacoustic noise emission.

543

544 Future work will deal with several of the listed limitations. A slightly smaller commercial wind turbine will be investigated
545 numerically with the presented approach and field measurements will be available for comparison. Subsequently, the turbine
546 will be simulated taking into account the operational conditions of the measurements. The influence of full shell coupling on
547 the low-frequency emission will be investigated in a future study. Based on the presented findings, constructional measures
548 as lattice towers, increased blade tower distance or swept blades are likely to reduce low-frequency emissions and should be
549 taken into account for future research.

550 *Data availability.* Data of the NREL 5 MW turbine is available from Jonkman et al. (2009).

551 *Competing interests.* The authors declare that they have no conflict of interest.

552 *Acknowledgements.* The studies ~~where~~ **Authors** ~~were~~ conducted as part of the joint research project "Objective Criteria for Seismic and
553 Acoustic Emission of Inland Wind Turbines (TremAc), FKZ 0325839A", funded by the German Federal Ministry for Economic Affairs and

Energy (BMW). The authors are grateful for the financial support. The authors gratefully acknowledge the *High Performance Computing* 554
Center Stuttgart for providing computational resources within the project *WEALoads*. 555

556 References

- 557 Arnold, M., Cheng, P. W., Biskup, F., et al.: Simulation of Fluid-Structure-Interaction on Tidal Current Turbines Based on Coupled Multibody
558 and CFD Methods, in: *The Twenty-third International Offshore and Polar Engineering Conference*, International Society of Offshore and
559 Polar Engineers, 2013.
- 560 Bekiropoulos, D., Lutz, T., Baltazar, J., Lehmkuhl, O., and Glodic, N.: D2013-3.1: Comparison of benchmark results from CFD-Simulation,
561 Deliverable report, KIC-OFFWINDTECH, 2013.
- 562 Bozorgi, A., Ghorbaniasl, G., and Nourbakhsh, S.: The reduction in low-frequency noise of horizontal-axis wind turbines by adjusting blade
563 cone angle, *International Journal of Environmental Science and Technology*, pp. 1–14, 2018.
- 564 Ghasemian, M. and Nejat, A.: Aerodynamic noise prediction of a horizontal Axis wind turbine using improved delayed detached eddy
565 simulation and acoustic analogy, *Energy Conversion and Management*, 99, 210–220, 2015.
- 566 Gortsas, T. V., Triantafyllidis, T., Chrisopoulos, S., and Polyzos, D.: Numerical modelling of micro-seismic and infrasound noise radiated by
567 a wind turbine, *Soil Dynamics and Earthquake Engineering*, 99, 108–123, 2017.
- 568 Hansen, K. L., Zajamšek, B., and Hansen, C. H.: The Occurrence of Nocturnal Wind Farm Rumbling Noise, *7th International Conference on*
569 *Wind Turbine Noise Rotterdam*, pp. 1–11, 2017.
- 570 Illg, J., Lutz, T., and Krämer, E.: Aeroacoustic Simulation of an Airfoil in Turbulent Inflow, in: *6th International Conference on Wind Turbine*
571 *Noise*, Glasgow, 2015.
- 572 Jassmann, U., Berroth, J., Matzke, D., Schelenz, R., Reiter, M., Jacobs, G., and Abel, D.: Model predictive control of a wind turbine modelled
573 in Simpack, in: *Journal of Physics: Conference Series*, vol. 524, IOP Publishing, 2014.
- 574 Jonkman, J., Butterfield, S., Musial, W., and Scott, G.: Definition of a 5-MW reference wind turbine for offshore system development, Tech.
575 rep., National Renewable Energy Lab.(NREL), Golden, CO (United States), 2009.
- 576 Knopper, L. D., Ollson, C. A., McCallum, L. C., Whitfield Aslund, M. L., Berger, R. G., Souweine, K., and McDaniel, M.: Wind turbines
577 and human health, *Frontiers in public health*, 2, 63, 2014.
- 578 Kowarsch, U., Keßler, M., and Krämer, E.: High order CFD-simulation of the rotor-fuselage interaction, in: *39th European Rotorcraft Forum*,
579 Moscow, 2013.
- 580 Kranzinger, P. P., Kowarsch, U., Schuff, M., Keßler, M., and Krämer, E.: Advances in parallelization and high-fidelity simulation of helicopter
581 phenomena, in: *High Performance Computing in Science and Engineering´ 15*, pp. 479–494, Springer, 2016.
- 582 Kroll, N., Rossow, C.-C., Becker, K., and Thiele, F.: The MEGAFLOW project, *Aerospace Science and Technology*, 4, 223–237, 2000.
- 583 Li, Y., Castro, A., Martin, J., Sinokrot, T., Prescott, W., and Carrica, P.: Coupled computational fluid dynamics/multibody dynamics method
584 for wind turbine aero-servo-elastic simulation including drivetrain dynamics, *Renewable Energy*, 101, 1037–1051, 2017.
- 585 Liu, W.: A review on wind turbine noise mechanism and de-noising techniques, *Renewable Energy*, 108, 311–320, 2017.
- 586 Luhmann, B., Seyedin, H., and Cheng, P.-W.: Aero-structural dynamics of a flexible hub connection for load reduction on two-bladed wind
587 turbines, *Wind Energy*, 20, 521–535, 2017.
- 588 Lutz, T., Arnold, B., Bekiropoulos, D., Illg, J., Krämer, E., Wolf, A., Hann, R., and Kamruzzaman, M.: Prediction of Flow-Induced Noise
589 Sources of Wind Turbines and Application Examples, *International Journal of Aeroacoustics*, 2015.
- 590 Madsen, H. A.: Low frequency noise from wind turbines mechanisms of generation and its modelling, *Journal of Low Frequency Noise*,
591 *Vibration and Active Control*, 29, 239–251, 2010.
- 592 Mann, J.: The spatial structure of neutral atmospheric surface-layer turbulence, *Journal of fluid mechanics*, 273, 141–168, 1994.

Matha, D., Hauptmann, S., Hecquet, T., and Kühn, M.: Methodology and results of loads analysis of wind turbines with advanced aeroelastic multi-body simulation, DEWEK, Bremen, 2010.	593 594
Menter, F. R.: Two-equation eddy-viscosity turbulence models for engineering applications, AIAA journal, 32, 1598–1605, 1994.	595
Pilger, C. and Ceranna, L.: The influence of periodic wind turbine noise on infrasound array measurements, Journal of Sound and Vibration, 388, 188–200, 2017.	596 597
Saccorotti, G., Piccinini, D., Cauchie, L., and Fiori, I.: Seismic noise by wind farms: a case study from the Virgo Gravitational Wave Observatory, Italy, Bulletin of the Seismological Society of America, 101, 568–578, 2011.	598 599
Sayed, M., Lutz, T., and Krämer, E.: Aerodynamic investigation of flow over a multi-megawatt slender bladed horizontal-axis wind turbine, Renewable Energies Offshore, 2015.	600 601
Sayed, M., Lutz, T., Krämer, E., Shayegan, S., Ghantasala, A., Wüchner, R., and Bletzinger, K.-U.: High fidelity CFD-CSD aeroelastic analysis of slender bladed horizontal-axis wind turbine, in: Journal of Physics: Conference Series, vol. 753, IOP Publishing, 2016.	602 603
Schepers, J., Ceyhan, O., Boorsma, K., Gonzalez, A., Munduate, X., Pires, O., Sørensen, N., Ferreira, C., Sieros, G., Madsen, J., Voutsinas, S., Lutz, T., Barakos, G., Colonia, S., Heielmann, H., Meng, F., and Croce, A.: Latest results from the EU project AVATAR: Aerodynamic modelling of 10 MW wind turbines, in: Journal of Physics: Conference Series, vol. 753, IOP Publishing, 2016.	604 605 606
Schuff, M., Kranzinger, P., Keler, M., and Krämer, E.: Advanced CFD-CSD coupling: Generalized, high performant, radial basis function based volume mesh deformation algorithm for structured, unstructured and overlapping meshes, in: Proceedings of the 40th European Rotorcraft Forum. Southampton. Great Britain, 2014.	607 608 609
Schulz, C., Klein, L., Weihing, P., and Lutz, T.: Investigations into the interaction of a wind turbine with atmospheric turbulence in complex terrain, in: Journal of Physics: Conference Series, vol. 753, p. 032016, IOP Publishing, 2016a.	610 611
Schulz, C., Meister, K., Lutz, T., and Krämer, E.: Investigations on the wake development of the MEXICO rotor considering different inflow conditions, in: New Results in Numerical and Experimental Fluid Mechanics X, pp. 871–882, Springer, 2016b.	612 613
Stammler, K. and Ceranna, L.: Influence of wind turbines on seismic records of the Gräfenberg array, Seismological Research Letters, 87, 1075–1081, 2016.	614 615
Streiner, S., Hauptmann, S., Kühn, M., and Krämer, E.: Coupled fluid-structure simulations of a wind turbine rotor, in: Deutsche Windenergie-Konferenz (DEWEK). Bremen, Germany: DEWI-German Wind Energy Institute, 2008.	616 617
Styles, P., Stimpson, I., Toon, S., England, R., and Wright, M.: Microseismic and infrasound monitoring of low frequency noise and vibrations from windfarms, Recommendations on the Siting of Windfarms in the Vicinity of Eskdalemuir, Scotland, Report to MOD/FTI/BWEA, 125pp, 2005.	618 619 620
Turnbull, C., Turner, J., and Walsh, D.: Measurement and level of infrasound from wind farms and other sources, Acoustics Australia, 40, 45–50, 2012.	621 622
Van den Berg, G.: The beat is getting stronger: the effect of atmospheric stability on low frequency modulated sound of wind turbines, Journal of Low Frequency Noise, Vibration and Active Control, 24, 1–23, 2005.	623 624
Viterna, L. A.: The NASA-LERC wind turbine noise prediction code, NASA CP, 2185, 1981.	625
Weihing, P., Letzgun, J., Bangga, G., Lutz, T., and Krämer, E.: Hybrid RANS/LES capabilities of the flow solver FLOWer-application to flow around wind turbines, in: The 6th Symposium on Hybrid RANS-LES Methods, Strassbourg, 2016.	626 627
Yauwenas, Y., Zajamek, B., Reizes, J., Timchenko, V., and Doolan, C. J.: Numerical simulation of blade-passage noise, The Journal of the Acoustical Society of America, 142, 1575–1586, 2017.	628 629

- 630 Zajamšek, B., Hansen, K. L., Doolan, C. J., and Hansen, C. H.: Characterisation of wind farm infrasound and low-frequency noise, Journal
631 of Sound and Vibration, 370, 176–190, 2016.
- 632 Zieger, T. and Ritter, J. R.: Influence of wind turbines on seismic stations in the upper rhine graben, SW Germany, Journal of Seismology,
633 22, 105–122, 2018.